nature geoscience

ARTICLES

PUBLISHED ONLINE: 19 DECEMBER 2016 | DOI: 10.1038/NGEO2861

Annual boom–bust cycles of polar phytoplankton biomass revealed by space-based lidar

Michael J. Behrenfeld[1]*, Yongxiang Hu[2], Robert T. O'Malley[1], Emmanuel S. Boss[3], Chris A. Hostetler[2], David A. Siegel[4], Jorge L. Sarmiento[5], Jennifer Schulien[1], Johnathan W. Hair[2], Xiaomei Lu[2], Sharon Rodier[2] and Amy Jo Scarino[2]

Polar plankton communities are among the most productive, seasonally dynamic and rapidly changing ecosystems in the global ocean. However, persistent cloud cover, periods of constant night and prevailing low solar elevations in polar regions severely limit traditional passive satellite ocean colour measurements and leave vast areas unobserved for many consecutive months each year. Consequently, our understanding of the annual cycles of polar plankton and their interannual variations is incomplete. Here we use space-borne lidar observations to overcome the limitations of historical passive sensors and report a decade of uninterrupted polar phytoplankton biomass cycles. We find that polar phytoplankton dynamics are categorized by 'boom–bust' cycles resulting from slight imbalances in plankton predator–prey equilibria. The observed seasonal-to-interannual variations in biomass are predicted by mathematically modelled rates of change in phytoplankton division. Furthermore, we find that changes in ice cover dominated variability in Antarctic phytoplankton stocks over the past decade, whereas ecological processes were the predominant drivers of change in the Arctic. We conclude that subtle and environmentally driven imbalances in polar food webs underlie annual phytoplankton boom–bust cycles, which vary interannually at each pole.

Ship- and aircraft-mounted Light Detection And Ranging (lidar) systems have been employed for decades to characterize ocean optical, phytoplankton, zooplankton, and fish properties[1–4]. However, global-scale plankton retrievals from a space-based lidar were first demonstrated only in 2013[5] with measurements from the Cloud-Aerosol Lidar with Orthogonal Polarization (CALIOP) sensor[6]. These active lidar measurements retrieve ocean plankton properties both day and night, penetrate between and through significant cloud cover, and have minimal atmospheric correction errors, thus addressing many limitations of passive ocean colour measurements particularly in polar regions[7]. Here we use 1°-latitude binned ocean particulate backscattering coefficients (b_{bp}) and diffuse attenuation coefficients (K_{D532}) determined from CALIOP's 532 nm polarization channels[5,8,9] to quantify phytoplankton biomass[10–12] in the surface mixed layer over the period 2006 to 2015 (Methods). CALIOP is a nadir-viewing sensor providing measurements along its orbit track to 81.5° latitude, with spatial coverage increasing with increasing latitude (Fig. 1c,g and Supplementary Fig. 1). Ocean properties retrieved by CALIOP are from its first 22.5 m vertical-resolution sampling bin below the surface[5]. Over its 16-day orbit repeat cycle, CALIOP views roughly 70% of the total 1°-resolution ocean bins poleward of 45° latitude (Supplementary Fig. 2).

Annual cycles in polar phytoplankton biomass

Before evaluating polar plankton properties, a 'comparison zone' of 45° to 55° latitude was defined where ocean observations are available throughout the year from both CALIOP and the Moderate-resolution Imagining Spectrometer (MODIS) passive ocean colour sensor (Fig. 1). For this comparison zone, we find an excellent agreement (north $r^2 = 0.84$, $n = 111$, $p < 0.001$; south $r^2 = 0.79$, $n = 111$, $p < 0.001$) between phytoplankton biomass cycles from the two sensors (Fig. 1d,h), which lends confidence to the CALIOP retrievals. During periods when polar data ($\geq$60° latitude) are also available from both sensors, we again find an excellent agreement (north $r^2 = 0.63$, $n = 84$, $p < 0.001$; south $r^2 = 0.81$, $n = 72$, $p < 0.001$) between MODIS and CALIOP (Supplementary Figs 3 and 4). In these polar zones, however, CALIOP continues to characterize phytoplankton biomass distributions right up to the ice edge (Fig. 1b,f) throughout the extended periods when MODIS data are entirely absent (for example, Fig. 1a,e). This advantage of active lidar sensing allows CALIOP to 'fill in' the late autumn to early-spring seasons hidden from ocean colour sensors and thus construct the first complete record of polar phytoplankton annual biomass cycles (Fig. 2a,c).

Phytoplankton concentrations retrieved by CALIOP in the northern and southern polar zones follow repeated winter-minimum and summer-maximum annual cycles, with secondary interannual variations in cycle amplitude (black symbols in Fig. 2a,c; range in amplitude of 24 to 45 mg C m^{-3} in the north and 11 to 21 mg C m^{-3} in the south) but no long-term trend ($p > 0.05$) over the CALIOP record. Throughout these time series, biomass changes show a clear correspondence ($r^2 = 0.78$) with mixed-layer phytoplankton division rates (μ; blue lines in Fig. 2a,c), calculated as:

$$\mu = \frac{\int_{t=\text{sunrise}}^{\text{sunset}} \int_{z=0}^{\text{MLD}} P^C_{\max} \tanh\left(\frac{\alpha^C \text{PAR}_{t,z}}{P^C_{\max}}\right) \text{d}z\, \text{d}t}{\text{MLD}} \quad (1)$$

[1]Department of Botany and Plant Pathology, Cordley Hall 2082, Oregon State University, Corvallis, Oregon 97331-2902, USA. [2]NASA Langley Research Center, MS 420, Hampton, Virginia 23681-2199, USA. [3]School of Marine Sciences, 5706 Aubert Hall, University of Maine, Orono, Maine 04469-5741, USA. [4]Earth Research Institute and Department of Geography, University of California, Santa Barbara, California 93106-3060, USA. [5]Atmospheric and Oceanic Sciences Program, 300 Forrestal Road, Sayre Hall, Princeton University, Princeton, New Jersey 08544, USA. *e-mail: mjb@science.oregonstate.edu

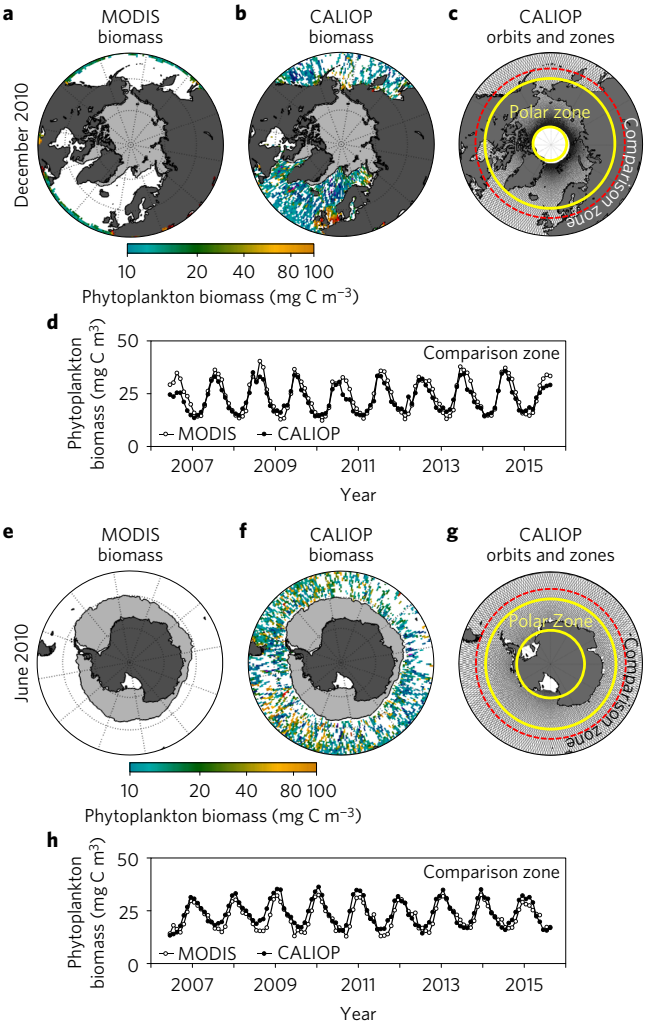

Figure 1 | Phytoplankton biomass observations from CALIOP and MODIS. **a**, MODIS phytoplankton biomass retrievals poleward of 45° latitude (white: no data) for northern latitudes (December 2010). **b**, CALIOP phytoplankton biomass retrievals for December 2010. **c**, Black lines: CALIOP orbit tracks poleward of 45° latitude. The red dashed ring demarks the 45°–55° 'comparison zone'. Yellow rings demark the north polar zone (60°–81.5° latitude). **d**, 2006–2015 monthly mean phytoplankton biomass for the north 'comparison zone'. **e**–**h**, As in **a**–**d**, respectively, but for southern latitudes during June 2010 (south polar zone in **f**: 60°–75°). Grey shading: ice cover in panels **a**,**b** and **e**,**f**.

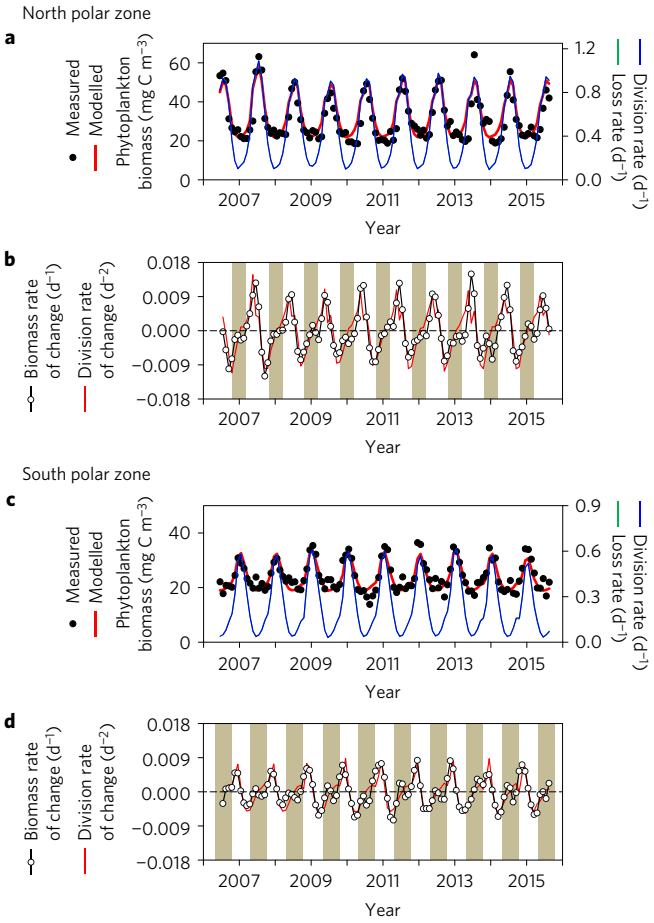

Figure 2 | Polar phytoplankton cycles. **a**,**c**, Black symbols: CALIOP monthly mean phytoplankton biomass (C). Blue line: phytoplankton division rates (μ). Green line: phytoplankton loss rates (l, which are indistinguishable from μ). Red line: calculated C time series from model predictions of $d\mu/dt$ (Methods). **b**,**d**, Open symbols, black line: biomass rates of change (r) calculated from CALIOP observations (equation (2)). Red line: modelled $d\mu/dt$ (equations (1) and (3)). Statistics on relationships between r and $d\mu/dt$ are: $r^2 = 0.63$, $n = 110$, $p < 0.001$ (**b**) and $r^2 = 0.71$, $n = 110$, $p < 0.001$ (**d**). Vertical tan bars: months with no MODIS data.

where, MLD is mixed-layer depth (m), $PAR_{t,z}$ is photosynthetically active radiation at time t and depth z, and α^C and P^C_{max} are the carbon-specific light-limited and light-saturated rates of photosynthesis (Methods). This correlation between biomass and division rate, however, does not imply that rapid division causes high biomass.

Temporal changes in phytoplankton concentration (C, mg C m^{-3}) reflect imbalances between division and loss (grazing, viral lysis, and so on) rates. This disequilibrium is quantified for a given time interval, t_0 to t_1, through the specific rate of biomass change (r; d^{-1}) (refs 13,14):

$$r = \frac{\ln\left(\frac{C_{t_1}}{C_{t_0}}\right)}{t_1 - t_0} \quad (2)$$

For both the north and south polar zones, the annual cycle in r shows that the spring increase in phytoplankton concentration begins (that is, r first becomes positive) when division rates are near their annual minimum (Fig. 3; purple dashed arrows). At the other extreme, bloom termination (that is, r first becomes negative) occurs when division rates are maximal (Fig. 3; green dashed arrows). Furthermore, the most rapid rate of biomass increase in spring (Fig. 3; black dashed arrows) coincides with division rates equivalent to those in autumn when biomass is most rapidly declining (Fig. 3; brown dashed arrows). These findings clearly demonstrate that the absolute rate of division defines neither the rate nor sign of biomass change.

The seemingly inconsistent annual cycles in polar biomass and division rate (Fig. 3) are reconciled if, as is the case for planktonic food webs[13–15], phytoplankton loss rates (l; d^{-1}) are closely coupled to, but slightly time-lagged behind, phytoplankton division rates (μ) (ref. 15) (Fig. 2a,c). For a time lag of 1 day (that is, $l_{t_1} = \mu_{t_0}$ and $t_1 - t_0 = \Delta t = 1$ day), the specific rate of change in biomass (r) is then determined by the rate of change in division ($d\mu/dt$; d^{-2}):

$$r_{t1} = \mu_{t1} - l_{t1} = \mu_{t1} - \mu_{t_0} = \frac{d\mu}{dt}\Delta t \quad (3)$$

This relationship clearly emerges from the CALIOP record, where we find highly correlated and comparable magnitude annual cycles in $d\mu/dt$ and r for both polar zones (Figs 2b,c and 3 top panels,

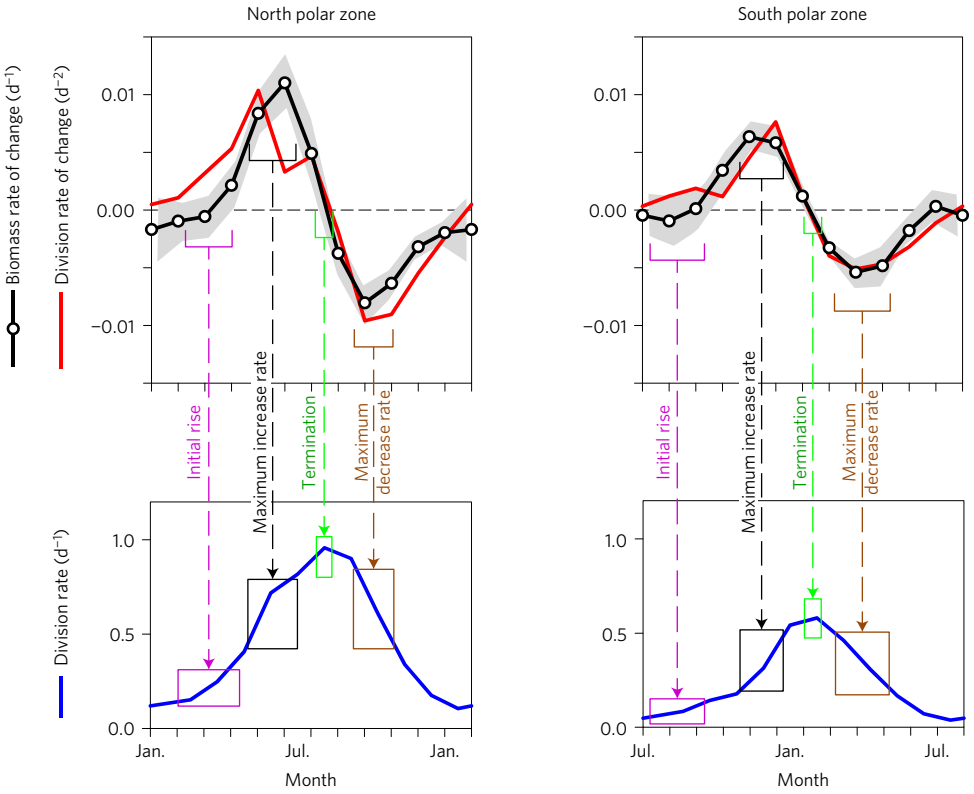

Figure 3 | Climatological annual phytoplankton cycles. Top panels: open symbols, black line: CALIOP-observed biomass change rate (r, grey shading indicates ±1 s.d.). Red line: modelled $d\mu/dt$ (equations (1) and (3)). The horizontal dashed line demarks $r=0$. Below this line biomass is decreasing, while above this line biomass is increasing. Bottom panels: annual cycles in division rate. Top and bottom panels are connected by four key events: purple arrow: initial rise in biomass; black arrow: maximum biomass increase rate; green arrow: bloom termination; brown arrow: maximum rate of biomass decline. Upper brackets indicate month range of event. Lower boxes indicate range in μ for each event (Methods).

Methods). Thus, the blooming phase of the annual cycle begins when division rates are minimal but accelerating (that is, $d\mu/dt$ is positive) and then ends when division reaches its maximum rate (that is, acceleration stops)[15] (Fig. 3). Conversely, the declining phase of the annual cycle results from a deceleration in division rate (that is, $d\mu/dt$ is negative)[15], despite absolute rates of division being comparable to those during the blooming phase (Fig. 3).

Our results indicate that the large-amplitude biomass cycles of polar systems (Fig. 2a,c) are a consequence of division and loss rates being perpetually decoupled through environmental changes in upper-ocean growth conditions. By extension, it may be anticipated that interannual variations in biomass cycles will likewise reflect environmentally controlled changes in annual minimum–maximum ranges for division rate (that is, the ability for division to accelerate and decelerate). This prediction is confirmed in the CALIOP record for the north and south polar regions, where 75% ($n = 34$, $p < 0.001$) of the interannual differences in minimum-to-maximum and maximum-to-minimum biomass change rates (equation (2)) are accounted for by our modelled ranges in $d\mu/dt$ (equations (1) and (3)) (Fig. 2b,c). The fidelity of this finding is further verified when modelled $d\mu/dt$ values are applied to initial phytoplankton concentrations for the north and south polar zones and the entire decade of CALIOP-observed biomass changes are effectively recaptured (north $r^2 = 0.78$, $n = 111$, $p < 0.001$; south $r^2 = 0.81$, $n = 111$, $p < 0.001$) without any additional 'restoring' of the modelled time series to measured values (red line in Fig. 2a,c).

Interannual variations in polar phytoplankton biomass

Variations in phytoplankton concentration are only one factor impacting the broader biogeochemistry of the polar oceans. A second critical property is the extent of ice-free ocean area (IFA)[16–19], with long-term trends in IFA (Supplementary Fig. 4) serving as harbingers of climate change. During the recent era of CALIOP measurements, seasonal anomalies in polar-zone integrated phytoplankton stocks (ΣC_{polar}; Fig. 4 black symbols) have spanned similar ranges in the north (3.2 Tg C) and south (2.4 Tg C), but for different reasons. In the north, seasonal anomalies in mean phytoplankton concentration (mg C m^{-3}) have dominated ΣC_{polar} variability (Fig. 4c; $r^2 = 0.80$, $n = 37$, $p < 0.001$), whereas IFA anomalies have driven variability in the south polar zone (Fig. 4b; $r^2 = 0.72$, $n = 37$, $p < 0.001$) (Supplementary Table 1). One reason for this difference is that surface nutrients in the polar north are often not fully depleted at the bloom climax, implying a potential for enhanced division rates during favourable years. In the south, the prevalence of iron-limiting conditions[20,21] is likely to play a key role in constraining anomalies in phytoplankton concentration (Fig. 4d). The second reason for the north–south difference is that IFA anomalies in the polar north were small over the CALIOP era (Fig. 4a), whereas changes in the polar south were the largest since the beginning of satellite ice-cover record in 1978 (Supplementary Fig. 5). These contrasting results for the two polar biomes highlight the importance of both ecological processes (for example, light, nutrients, grazing controls) and physical properties (for example, ice cover) in regulating plankton stocks and raise questions on what these changes observed today imply about polar ecosystem trajectories into the future.

Extending knowledge on planktonic ecosystems

Advantages of active satellite lidar sensing have enabled uninterrupted monitoring of polar plankton populations since 2006. Our CALIOP-based analysis provides the strongest observational

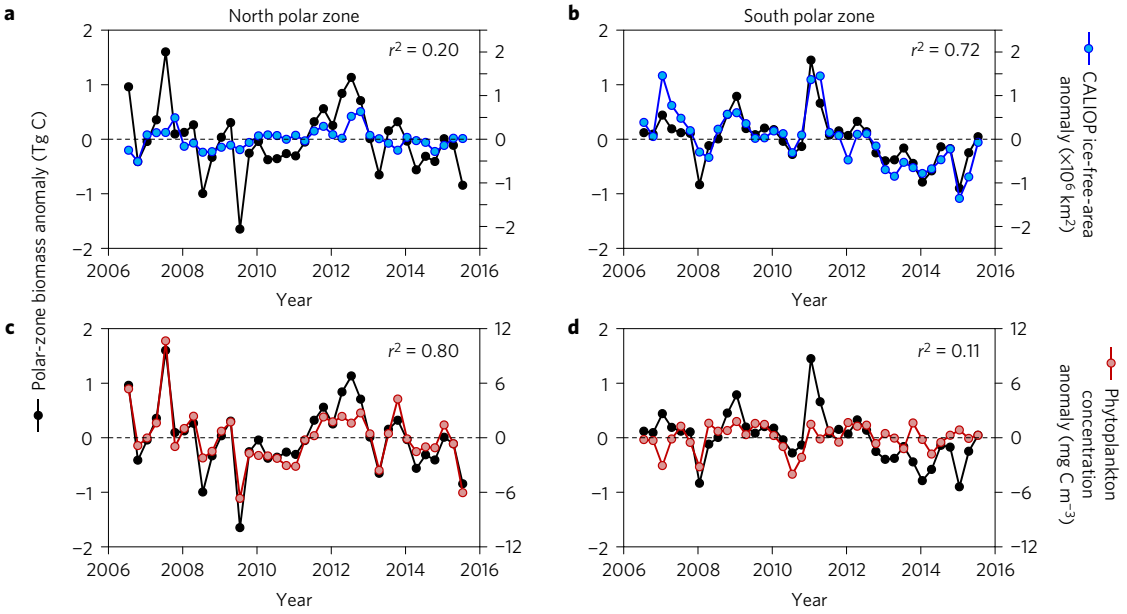

Figure 4 | Interannual changes in polar-zone phytoplankton biomass. Black symbols, black line: seasonal anomalies in polar-zone integrated photic-layer phytoplankton biomass (ΣC_{polar} = phytoplankton concentration (mg C m^{-3}) × photic-zone depth (m) × IFA (m^2)/10^{12} mg Tg^{-1}). **a**,**b**, Blue symbols, blue line: ice-free-area (IFA) seasonal anomalies. **c**,**d**, Red symbols, red line: phytoplankton concentration seasonal anomalies. Anomalies are calculated as the difference between a property value for a given season and the average value for that season over the 2006 to 2015 CALIOP era. Seasons: December–February, March–May, June–August and September–November.

evidence to date that large-scale variability in polar phytoplankton concentrations is governed by the extent to which mixed-layer growth conditions allow division rates to accelerate or decelerate in time[15]. The temporal lag between phytoplankton division and loss rates implied by our data is on the order of days (Methods), but further studies are necessary to evaluate whether such tight predator–prey coupling operates at finer space and time scales. The finding that annual polar blooms terminate when division rates are maximal (Figs 2 and 3) is consistent with an earlier proposal regarding global phytoplankton biomass dynamics[15] and may provide additional insight into phytoplankton community structure during a bloom. Specifically, if our current results for total phytoplankton biomass can be extended to the species level, then an implication is that species with high light-use efficiencies and low maximum growth rate potentials will have an initial advantage under low-light conditions, but will saturate in division early during the blooming phase and thus soon be overcome by losses. On the other hand, species with high potential growth rates can continue to accelerate division ahead of loss rates and, accordingly, may ultimately come to dominate biomass at the bloom climax. Consistent with this view, diatoms are often noted for their exceptionally high division potentials[22–24] and their frequent dominance of climax bloom populations[25–27]. Extending this thought further, it might also be speculated that the dominance of diatoms is more likely when rapid division rates are permitted, but under less favourable bloom conditions other species may emerge as dominants in the climax community.

Despite being designed for atmospheric (not oceanographic) research, CALIOP measurements have here revealed previously unobserved early stages of polar plankton blooms, provided new insights into mechanisms driving annual boom–bust cycles and interannual variability in plankton stocks, and established a comparative baseline for future regionally focused analyses. The full potential of satellite lidar technology for polar research is, however, yet to be realized. With today's technology, airborne lidar systems retrieve vertically resolved (3–5 m resolution) plankton properties to nearly 3 optical depths[28], measure plankton absorption and scattering separately[29], and detect physiological properties of the phytoplankton[30]. By extending such capabilities to space and combining these measurements with passive satellite ocean colour data and *in situ* depth-profiling autonomous measurements, an observational infrastructure is foreseeable that enables three-dimensional reconstructions of polar-to-global ocean ecosystems and provides new insights into ocean ecology, biogeochemistry, and physical–biological interactions relevant to climate change research.

Methods

Methods, including statements of data availability and any associated accession codes and references, are available in the online version of this paper.

Received 9 June 2016; accepted 18 November 2016; published online 19 December 2016

References

1. Hoge, F. E. *et al*. Airborne lidar detection of subsurface oceanic scattering layers. *Appl. Opt.* **27,** 3969–3977 (1988).
2. Churnside, J. H., Sawada, K. & Okumura, T. A comparison of airborne lidar and echo sounder performance in fisheries. *J. Mar. Acoust. Soc. Jpn* **28,** 175–183 (2001).
3. Churnside, J. H. & Thorne, R. E. Comparison of airborne lidar measurements with 420 kHz echo-sounder measurements of zooplankton. *Appl. Opt.* **44,** 5504–5511 (2005).
4. Dickey, T. D., Kattawar, G. W. & Voss, K. J. Shedding new light on light in the ocean. *Phys. Today* **64,** 44–49 (April, 2011).
5. Behrenfeld, M. J. *et al*. Space-based lidar observations of global ocean plankton populations. *Geophys. Res. Lett.* **40,** 4355–4360 (2013).
6. Winker, D. M. *et al*. Overview of the CALIPSO Mission and CALIOP data processing algorithms. *J. Atmos. Ocean. Technol.* **26,** 2310–2323 (2009).
7. Babin, M. & Forget, M.-H. in *Ocean Colour Remote Sensing of Polar Regions* (eds Babin, M., Arrigo, K., Bélanger, S. & Forget, M.-H.) Ch. 1 (Reports of the Ocean Colour Coordinating Group, IOCCG, 2015).
8. Churnside, J. H., McCarty, B. J. & Lu, X. Subsurface ocean signals from an orbiting polarization lidar. *Remote Sens.* **5,** 3457–3475 (2013).
9. Lu, X., Hu, Y., Trepte, C., Zeng, S. & Churnside, J. H. Ocean subsurface studies with the CALIPSO spaceborne lidar. *J. Geophys. Res.* **119,** 4305–4317 (2014).

10. Behrenfeld, M. J., Boss, E., Siegel, D. A. & Shea, D. M. Carbon-based ocean productivity and phytoplankton physiology from space. *Glob. Biogeochem. Cycles* **1,** GB1006 (2005).
11. Westberry, T. K., Behrenfeld, M. J., Siegel, D. A. & Boss, E. Carbon-based primary productivity modeling with vertically resolved photoacclimation. *Glob. Biogeochem. Cycles* **22,** GB2024 (2008).
12. Graff, J. R. *et al*. Analytical phytoplankton carbon measurements spanning diverse ecosystems. *Deep-Sea Res.* **102,** 16–25 (2015).
13. Behrenfeld, M. J. & Boss, E. S. Resurrecting the ecological underpinnings of ocean plankton blooms. *Ann. Rev. Mar. Sci.* **6,** 167–194 (2014).
14. Evans, G. T. & Parslow, J. S. A model of annual plankton cycles. *Biol. Oceanogr.* **3,** 327–347 (1985).
15. Behrenfeld, M. J. Climate-mediated dance of the plankton. *Nat. Clim. Change* **4,** 880–887 (2014).
16. Stroeve, J. C. *et al*. Trends in Arctic sea ice extent from CMIP5, CMIP3 and observations. *Geophys. Res. Lett.* **39,** 16, L16502 (2012).
17. Cavalieri, D. J., Gloersen, P., Parkinson, C., Comiso, J. & Zwally, H. J. Observed hemispheric asymmetry in global sea ice changes. *Science* **278,** 1104–1106 (1997).
18. Arrigo, K. R. & van Dijken, G. L. Continued increases in Arctic Ocean primary production. *Prog. Oceanogr.* **136,** 60–70 (2015).
19. Arrigo, K. R., van Dijken, G. L. & Bushinsky, S. Primary production in the Southern Ocean, 1997–2006. *J. Geophys. Res.* **113,** C08004 (2008).
20. Boyd, P. W. *et al*. Mesoscale iron enrichment experiments 1993–2005: synthesis and future directions. *Science* **315,** 612–617 (2007).
21. de Baar, H. J. W. *et al*. Synthesis of iron fertilization experiments: from the Iron Age in the Age of Enlightenment. *J. Geophys. Res.* **110,** C09S16 (2005).
22. Ichimi, K., Kawamura, T., Yamamoto, A., Tada, K. & Harrison, P. J. Extremely high growth rate of the small diatom *Chaetoceros salsugineum* isolated from an estuary in the eastern Seto inland sea, Japan. *J. Phycol.* **48,** 1284–1288 (2012).
23. Furnas, M. J. *In situ* growth rates of marine phytoplankton: approaches to measurement, community and species growth rates. *J. Plank. Res.* **12,** 1117–1151 (1990).
24. Brand, L. E. & Guillard, R. R. L. The effects of continuous light and light intensity on the reproduction rates of twenty-two species of marine phytoplankton. *J. Exp. Mar. Biol. Ecol.* **50,** 119–132 (1981).
25. Mahadevan, A., D'Asaro, E., Lee, C. & Perry, M. J. Eddy-driven stratification initiates North Atlantic spring phytoplankton blooms. *Science* **337,** 54–58 (2012).
26. Coale, K. H. *et al*. A massive phytoplankton bloom induced by an ecosystem-scale iron fertilization experiment in the equatorial Pacific Ocean. *Nature* **383,** 495–501 (1996).
27. Irigoien, X., Harris, R. P., Head, R. N. & Harbour, D. North Atlantic Oscillation and spring bloom phytoplankton composition in the English Channel. *J. Plankton Res.* **22,** 2367–2371 (2000).
28. Hair, J. H. *et al*. Airborne high spectral resolution lidar for profiling aerosol optical properties. *Appl. Opt.* **47,** 6734–6752 (2008).
29. deRada, S., Ladner, S. & Arnone, R. A. Coupling ocean models and satellite derived optical fields to estimate lidar penetration and detection performance. *Proc. SPIE* **8532,** 85320T-1 (2012).
30. Hoge, F. E., Lyon, P. E., Wright, C. W., Swift, R. N. & Yungel, J. K. Chlorophyll biomass in the global oceans: airborne lidar retrieval using fluorescence of both chlorophyll and chromophoric dissolved organic matter. *Appl. Opt.* **44,** 2857–2862 (2005).

Acknowledgements

This work was supported by the National Aeronautics and Space Administration's Ocean Biology and Biogeochemistry Program and the North Atlantic Aerosol and Marine Ecosystems Study (NAAMES).

Author contributions

M.J.B. designed the study; M.J.B., Y.H. and R.T.O'M. processed satellite data and analysed results; M.J.B. and R.T.O'M. prepared display items; M.J.B. wrote the manuscript with contributions from all authors.

Additional information

Supplementary information is available in the online version of the paper. Reprints and permissions information is available online at www.nature.com/reprints. Correspondence and requests for materials should be addressed to M.J.B.

Competing financial interests

The authors declare no competing financial interests.

Methods

Global data sets. Particulate backscatter coefficients (b_{bp}) and photosynthetically active radiation (PAR) data from the MODIS Aqua ocean colour sensor for the period June 2006 to July 2015 were acquired from http://oceancolor.gsfc.nasa.gov/cms. MODIS Aqua b_{bp} values were based on the Generalized Inherent Optical Properties inversion algorithm (GIOP)[31]. CALIOP data for the June 2006 to July 2015 period were analysed as described in Behrenfeld *et al.*[5] except for the following modifications. First, the CALIPSO satellite has been tilted 30° off-nadir for one orbit every two weeks since September 2015 to collect ocean measurements with minimal surface backscatter. These observations have allowed for an improved description of depolarization ratios among ocean subsurface backscatter, diffuse attenuation coefficients, and b_{bp} compared with the earlier study[5]. Second, collocated MODIS and CALIOP data were used to develop a relationship between diffuse attenuation coefficients at 532 nm (K_{D532}) and b_{bp} to allow retrieval of b_{bp} at high latitudes from CALIOP measurements alone, whereas in Behrenfeld *et al.*[5] collocated MODIS K_{D532} data were required to retrieve b_{bp}.

CALIOP b_{bp} and K_{D532} measurements are collected at nadir along the satellite orbit track, with an ocean surface lidar single-pulse footprint of ~100 m and an along-track pulse-to-pulse distance of 330 m. Ocean properties are retrieved along CALIOP orbit tracks only for cloud layers <1 optical depth. Over a 16-day repeat cycle, CALIOP measurement tracks (day and night) are separated by 0 to 1.5°. Given these differences in along-track and between-track coverage, CALIOP data were aggregated into monthly 1° latitude bins for comparison with MODIS spatial coverage (Supplementary Fig. 2). For all other analyses, CALIOP data were aggregated into broader latitude zones, such as the 'comparison zones' (45° to 55° latitude, Fig. 1c,g) and the polar zones of the Northern (60°–81.5° latitude) and Southern (60°–75° latitude) hemispheres. CALIOP b_{bp} values were multiplied by 1.3 to scale with MODIS b_{bp} values, thus illustrating the close correspondence between annual cycles retrieved by these two sensors. In the analysis of Behrenfeld *et al.*[5], an excellent agreement was found between *in situ* measured b_{bp} and unscaled CALIOP b_{bp} values, whereas b_{bp} values retrieved with the Garver–Siegel–Maritorena inversion algorithm[32] (GIOP products were not available at the time of the earlier study) were a factor of 1.3 higher than both the *in situ* and CALIOP data. The reason for this discrepancy is not yet resolved, but for the current study derived biomass accumulation rates (r) are little impacted by whether the CALIOP data are scaled to MODIS data or vice versa. Future analyses identifying the basis for this bias between sensor retrievals will be important for improving quantitative assessments of polar phytoplankton carbon standing stocks. Finally, CALIOP, MODIS, and all other satellite ocean colour sensors fail to detect phytoplankton populations under ice, so the contribution of these populations is not represented in any satellite assessment of polar phytoplankton stocks.

CALIOP and MODIS b_{bp} values were converted to C_{phyto} (mg C m^{-3}) following (Supplementary Discussion) (refs 10,12):

$$C_{phyto} = 12{,}128\ \text{mg C m}^{-2}(b_{bp} - 0.00035\ \text{m}^{-1}) \quad (4)$$

CALIOP K_{D532} values were converted to diffuse attenuation coefficients for PAR (K_{PAR}, m^{-1}) (ref. 33) and photic-layer depth (Z_{eu}, m) was taken as the depth of the 0.415 mol quanta m^{-2} d^{-1} isolume[34,35] and calculated as $Z_{eu} = \ln(0.415/\text{PAR})/K_{PAR}$, except during polar night when Z_{eu} was assigned a value of 1 m. For calculations of integrated photic-zone biomass (ΣC_{polar}), we assume that biomass is distributed uniformly with depth and equal to the value observed at the surface. Field studies have shown that subsurface chlorophyll maxima are common in polar regions[1]. These features are not detected by satellite sensors and accordingly will cause our estimates of ΣC_{polar} to be conservative. Day length values were calculated as a function of date and latitude following Kirk[36]. Mixed-layer depths (MLDs) were calculated from salinity, temperature, and pressure data converted to density (sigma-theta) and based on the Fleet Numerical Meteorology and Oceanography Center (FNMOC) high-resolution ocean analysis model[37] for the period 2006–2007 and the HYbrid Coordinate Ocean Model (HYCOM) (https://hycom.org) for the period 2008–2015. The FNMOC and HYCOM models are both tuned to *in situ* data (that is, they are 'data-assimilating models'). The FNMOC model does not provide MLD data at latitudes >70° so monthly climatological average MLD data from the HYCOM model were applied at >70° latitude for the years 2006 and 2007. Results presented for the current manuscript are based on mixed-layer depths defined as a density change of 0.030 kg m^{-3} from the value at 10 m (ref. 38). Alternative definitions of MLD were evaluated and resulted in small decreases, but similar annual cycles, in modelled values of μ as the MLD criterion was increased from 0.005 to 0.125 kg m^{-3}, with small impacts on values of $d\mu/dt$ and its relationship with biomass accumulation rates, r. Ice-free ocean area for latitudes >60° was based on monthly Sea Ice Index extent data obtained from the National Snow and Ice Data Center (NSIDC) in Boulder, Colorado.

Assessment of phytoplankton division and accumulation rates. Daily net primary production (ΣNPP, mg C m^{-2} d^{-1}) was calculated for the mixed layer as a function of time and depth following:

$$\Sigma\text{NPP} = \int_{t=\text{sunrise}}^{\text{sunset}} \int_{z=0}^{\text{MLD}} CP^{C}_{\max} \tanh\left(\frac{\alpha^{C}\text{PAR}_{t,z}}{P^{C}_{\max}}\right) dz\, dt \quad (5)$$

where C is CALIOP-retrieved phytoplankton concentration (mg C m^{-3}) and is assumed to be uniform through the mixed layer, MLD is mixed-layer depth (m), and $\text{PAR}_{t,z}$ is photosynthetically active radiation (mol photon m^{-2} h^{-1}) at time t and depth z. Equation (5) was operated at 1 m depth increments and 64 time increments over the photoperiod. Temporal changes in incident PAR at the sea surface were modelled as a cosine function of time such that the integral of PAR_t for the photoperiod equalled the MODIS cloud-corrected PAR product. $\text{PAR}_{t,z}$ was calculated as $\text{PAR}_{t,z} = \text{PAR}_t e^{-K_{PAR} z}$. The carbon-specific light-saturated rate of photosynthesis, $P^{C}_{\max}$ (mg C (mg C h)$^{-1}$), was calculated as the product of the chlorophyll-specific light-saturated rate of photosynthesis, $P^{b}_{\max}$ (mg C (mg Chl h)$^{-1}$), and the phytoplankton Chl/C ratio (mg mg^{-1}). $P^{b}_{\max}$ was calculated as a function of sea surface temperature (SST) following an exponential relationship[39] with a Q_{10} of 2 (ref. 40). Chl/C values were calculated following the model of Behrenfeld and colleagues[41]. The light-saturation parameter, E_k (mol photon m^{-2} h^{-1}), was then calculated from Chl/C (ref. 41) and the carbon-specific light-limited slope of the photosynthesis–irradiance relationship, α^{C} (mg C m^2 (mg C mol photon)$^{-1}$), calculated as $P^{C}_{\max}/E_k$. Phytoplankton division rates (μ) were calculated as $\Sigma\text{NPP}/\Sigma C_{ML}$, where ΣC_{ML} is the mixed-layer integrated phytoplankton biomass, $C \times$ MLD. Phytoplankton concentration, C, cancels from the numerator and denominator when equation (5) is divided by ΣC_{ML}, thus leaving the simplified expression for μ given as equation (1). Thus, variability in μ and its temporal derivative, $d\mu/dt$, is determined by time-dependent changes in MLD, PAR, K_{PAR}, and SST (owing to the dependence of $P^{C}_{\max}$ on SST). 2006 through 2015 time series of MLD, PAR, SST and Z_{eu} are provided in Supplementary Fig. 6.

Figure 2b,c compares for the north and south polar zones observed rates of change in phytoplankton biomass (r) and values of $d\mu/dt$ calculated as:

$$d\mu/dt = \frac{\mu_{t_1} - \mu_{t_0}}{t_1 - t_0} \quad (6)$$

where $t_1 - t_0 = 1$ month (see Supplementary Discussion for analysis of uncertainty). We show that r and $d\mu/dt$ have correlated annual cycles of comparable magnitude, implying that phytoplankton loss rates are time-lagged behind division rates by ~1 day when averaged over a monthly period. This result does not mean that a 1 day lag will necessarily be observed between division and loss rates when measured on a daily timescale.

Figure 2a,b compares observed and modelled time series of phytoplankton biomass. Modelled phytoplankton biomass in this comparison (red line) was calculated by assigning an initial biomass of 45 and 20 mg C m^{-3} for the polar north and south, respectively, and then applying the model predictions of $d\mu/dt$ (that is, the derivative of equation (1)) over the 10-year time series.

While an excellent correspondence is observed between the CALIOP time series of r and $d\mu/dt$ for both polar zones, there are also secondary discrepancies. For example, observed values of r were notably higher than calculated values of $d\mu/dt$ during May and June of 2013 for the north polar zone. Such discrepancies can arise for multiple reasons, including errors in the observational data, comparison of monthly satellite biomass data with differences in spatial coverage, uncertainties in modelled values of $d\mu/dt$ associated with errors in input data fields (for example, MLD, PAR, K_{PAR}, and SST), or unaccounted for temporal variations in phytoplankton physiological properties and loss processes. Differences between observed r and modelled $d\mu/dt$ are responsible for mismatches between measured and modelled biomass values (Fig. 2a,c).

Phytoplankton climatological annual cycles. Figure 3 shows climatological average monthly cycles of (top panels) phytoplankton biomass accumulation rates (r), modelled $d\mu/dt$, and (bottom panels) phytoplankton division rates (μ). For these data, linear regression statistics for the r versus $d\mu/dt$ relationships are $r^2 = 0.72$, $n = 12$, $p < 0.001$ for the north polar zone and $r^2 = 0.85$, $n = 12$, $p < 0.001$ for the south polar zone. In the figure, the top and bottom panels are connected for four key events. Here, the initial rise in biomass (purple dashed arrows) was taken as the point where the biomass rate of change first becomes positive and thereafter remains positive to the bloom climax. For each arrow, the ranges in r (coloured brackets in top panels) and μ (boxes in the bottom panels) are taken from the year-by-year occurrences of these events shown in Fig. 2.

Data availability. Remote sensing data on ocean plankton properties and surface mixed-layer depth used in this study are available at http://oceancolor.gsfc.nasa.gov/cms and http://www.science.oregonstate.edu/ocean.productivity and from the corresponding author on request. Ice-cover data are available at https://nsidc.org.

References

31. Werdell, P. J. *et al*. Generalized ocean color inversion model for retrieving marine inherent optical properties. *Appl. Opt.* **52,** 2019–2037 (2013).
32. Maritorena, S., Siegel, D. A. & Peterson, A. R. Optimization of a semianalytical ocean color model for global-scale applications. *Appl. Opt.* **41,** 2705–2714 (2002).
33. Morel, A. *et al*. Examining the consistency of products derived from various ocean color sensors in open ocean (Case 1) waters in the perspective of a multi-sensor approach. *Remote Sens. Environ.* **111,** 69–88 (2007).
34. Boss, E. & Behrenfeld, M. J. *In-situ* evaluation of the initiation of the North Atlantic phytoplankton bloom. *Geophys. Res. Lett.* **37,** L18603 (2010).
35. Letelier, R. M., Karl, D. M., Abbott, M. R. & Bidigare, R. R. Light driven seasonal patterns of chlorophyll and nitrate in the lower euphotic zone of the North Pacific Subtropical Gyre. *Limnol. Oceanogr.* **49,** 508–519 (2004).
36. Kirk, J. T. O. *Light and Photosynthesis in Aquatic Ecosystems* (Cambridge Univ. Press, 1994).
37. Cummings, J. A. Operational multivariate ocean data assimilation. *Q. J. R. Meteorol. Soc.* **131,** 3583–3604 (2005).
38. de Boyer Montégut, C., Madec, G., Fischer, A. S., Lazar, A. & Iudicone, D. Mixed layer depth over the global ocean: an examination of profile data and a profile-based climatology. *J. Geophys. Res.* **109,** C12003 (2004).
39. Antoine, D., André, J.-M. & Morel, A. Oceanic primary production 2. Estimation at global scale from satellite (coastal zone color scanner) chlorophyll. *Glob. Biogeochem. Cycles* **10,** 57–69 (1996).
40. Eppley, R. W. Temperature and phytoplankton growth in the sea. *Fish. Bull.* **70,** 1063–1085 (1972).
41. Behrenfeld, M. J. *et al*. Revaluating ocean warming impacts on global phytoplankton. *Nat. Clim. Change* **6,** 323–330 (2016).